ACS APPLIED MATERIALS & INTERFACES

www.acsami.org

Research Article

Efficient and Tunable Luminescence in $Ga_{2-x}In_xO_3:Cr^{3+}$ for Near-Infrared Imaging

Jiyou Zhong, Ya Zhuo, Fu Du,* Hongshi Zhang, Weiren Zhao,* and Jakoah Brgoch*

Cite This: *ACS Appl. Mater. Interfaces* 2021, 13, 31835−31842

Read Online

ACCESS | Metrics & More | Article Recommendations | Supporting Information

ABSTRACT: Broadband near-infrared (NIR) emitting materials are in great demand as next-generation smart NIR light sources. In this work, a Cr^{3+}-substituted phosphor capable of efficiently converting visible to NIR light is developed through the solid solution, $Ga_{2-x}In_xO_3:Cr^{3+}$ ($0 \le x \le 0.5$). The compounds were prepared using high-temperature solid-state synthesis, and the crystal and electronic structure, morphology, site preference, and photoluminescence properties are studied. The photoluminescence results demonstrate a high quantum yield (88%) and impressive absorption efficiency (50%) when $x = 0.4$. The NIR emission is tunable across a wide range (713−820 nm) depending on the value of x. Moreover, fabricating a prototype of a phosphor-converted NIR light-emitting diode (LED) device using 450 nm LED and the $[(Ga_{1.57}Cr_{0.03})In_{0.4}]O_3$ phosphor showed an output power that reached 40.4 mW with a photoelectric conversion efficiency of 25% driven by a current of 60 mA, while the resulting device was able to identify damaged produce that was undetectable using visible light. These results demonstrate the outstanding potential of this phosphor for NIR LED imaging applications.

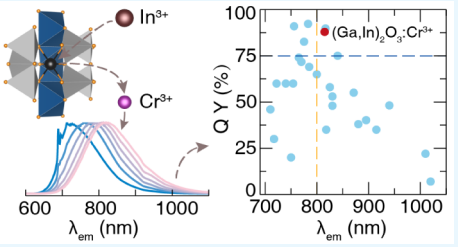

KEYWORDS: *pc-NIR LEDs, phosphor, luminescence, broadband, solid solution*

1. INTRODUCTION

Broadband near-infrared (NIR) luminescent materials emitting in the 700−1100 nm range have gained recent attention owing to their widespread need in food quality testing and analysis, night vision, and the medical diagnostic fields.[1−4] This wavelength window is also useful because NIR light can be transmitted through the first biological window allowing it to be used for deep tissue imaging and blood glucose sensing, among numerous other uses.[5,6] Most importantly, this wavelength region can be detected using inexpensive silicon detectors.[7] Despite the diverse set of applications and ease of detection, these analytical tests all require the generation of the NIR photons. There remains a need to create devices that can efficiently generate the NIR light. Recently, phosphor-converted NIR light-emitting diodes (pc-NIR LEDs) were shown to produce superior output power, high efficiency, durability, and compact size compared to traditional NIR light sources, such as incandescent bulbs, tungsten halogen lamps, or NIR LEDs. These advantages make pc-NIR LEDs ideal for low-cost and convenient spectroscopic applications.[8,9]

A pc-NIR LED operates by converting the highly efficient blue LED emission ($\lambda_{em} \approx 450$ nm) to the NIR region using an inorganic phosphor. Cr^{3+}-substituted materials are considered ideal NIR emitters for this process because their broadband excitation spectrum matches the LED output. The subsequent generation of either sharp-line, spin-forbidden ($^2E \rightarrow {}^4A_2$) Cr^{3+} transitions or broadband, spin-allowed ($^4T_2 \rightarrow {}^4A_2$) Cr^{3+} transitions occurs in the red or NIR region, depending on the crystal field splitting.[9−11] Trivalent chromium is particularly exciting because, unlike rare-earth ions, which tend to emit at shorter wavelengths,[12−14] substituting this ion into a weak octahedral crystal field environment will generate low-energy (red-shifted) spin-allowed electronic transitions.[15] As a result, various Cr^{3+}-activated broadband NIR phosphors have been developed with emission peaks ranging from 700 to 1100 nm.[16−22] Among them, the $Ca_3Sc_2Si_3O_{12}:Cr^{3+}$ ($\lambda_{em} = 783$ nm) and $Gd_3Sc_2Ga_3O_{12}:Cr^{3+}$ ($\lambda_{em} = 756$ nm) phosphors were reported to have a quantum yield (QY) above 90%,[23,24] and $LaMgGa_{11}O_{19}:Cr^{3+}$ ($\lambda_{em} = 775$ nm) has a QY of 83%,[25] showing a great potential in practical applications. However, the materials currently reported with an emission peak wavelength over 800 nm tend to suffer from a lower efficiency (QY < 80%).[26−30]

The simple oxide Ga_2O_3 was recently reported to exhibit a high QY (>90%), with the emission peak located at ∼715 nm when substituted with Cr^{3+}.[31] Although this material generates highly efficient NIR photoluminescence, the comparatively short emission wavelength limits its versatility. However, it is possible to partially substitute Ga^{3+} with various trivalent cations, which provides a chemical handle to tune the crystal field splitting by influencing the crystal structure. Indeed, the

Received: March 31, 2021
Accepted: June 15, 2021
Published: June 29, 2021

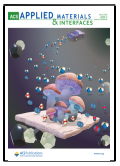

incorporation of larger ions such as Sc^{3+} or In^{3+} via solid solution substitution is likely to tune the luminescence toward a longer emission wavelength by reducing the crystal field splitting of Cr^{3+}. Moreover, synthesizing solid solutions allows the composition, structure, and luminescence properties of Cr^{3+}-activated phosphors to vary gradually and reveal new insight into these materials. Recently, Fang et al. reported a $(Ga,Sc)_2O_3:Cr^{3+}$ solid solution with a high efficiency and tunable NIR emission, demonstrating the outstanding performance of this material system.[32] As In^{3+} is larger than Sc^{3+} in ionic size, the weaker crystal field induced by In^{3+} could lead to the extension of the emission to longer wavelengths. In this regard, and considering the reported solubility of In^{3+} in Ga_2O_3,[33] a series of Cr^{3+}-substituted $Ga_{2-x}In_xO_3$ ($0 \le x \le 0.5$) phosphors were investigated. The solid solution of these compounds generated a high QY and tunable emission. The resulting structural and photoluminescence properties were then investigated through a combination of experiment and theoretical calculation to understand the fundamental crystal chemistry dictating the properties. Finally, the power conversion efficiency of transforming a blue LED (λ_{em} = 450 nm) to the NIR region was found to be excellent, with the potential of this new pc-NIR LED demonstrated in food analysis. These results highlight the potential of the $Ga_{2-x}In_xO_3:Cr^{3+}$ solid solution as a promising LED-excited NIR-emitting material that can be used for future imaging applications.

2. EXPERIMENTAL SECTION

2.1. Synthesis. $[(Ga_{1.97-x}Cr_{0.03})In_x]O_3$ (x = 0, 0.1, 0.2, 0.3, 0.4, and 0.5) solid solutions were prepared using a high-temperature, solid-state chemical route with Ga_2O_3 (Sigma-Aldrich, 99.95%), In_2O_3 (Sigma-Aldrich, 99.9%), and Cr_2O_3 (Sigma-Aldrich, 99.99%) employed as the starting materials. The powders were weighed according to the required stoichiometric ratio and ground using an agate mortar and pestle, and the homogeneous mixtures were placed in an alumina crucible. The mixtures were heated to 1300 °C with a heating rate of 3 °C/min and held for 6 h in air. The final products were ground into a fine powder using an agate mortar and pestle.

2.2. Characterization. X-ray diffractograms (X'Pert3 PANalytical; Cu Kα, λ = 1.5406 Å) were collected to confirm phase purity and determine the lattice parameters for each nominally loaded composition. Scanning electron microscopy (SEM) images and energy-dispersive X-ray spectroscopy (EDS) elemental mapping were collected on a Hitachi-S4800 (Japan). The room-temperature photoluminescence, temperature-dependent photoluminescence, and the time-gated photoluminescence decay curves of the Cr^{3+}-substituted compounds were all collected using an FLS-980 fluorescence spectrophotometer (Edinburgh Instruments) equipped with a Xenon flash lamp (450 W, Osram) excitation source. The QYs were measured using a Quantaurus-QY Plus C13534-11 (Hamamatsu Photonics). The diffuse reflectance (DR) spectra were detected on a UV−vis−NIR spectrophotometer (Shimadzu, Japan) with an integrated sphere attachment and $BaSO_4$ powder as a standard. The NIR LED device was fabricated by coating a mixture of the as-prepared $Ga_{1.57}In_{0.4}Cr_{0.03}O_3$ phosphor and resin with a 1:10 ratio in weight on a 460 nm blue LED. The electroluminescence spectrum, output power, and photoelectric conversion efficiency of the fabricated pc-NIR LED device were measured using a HAAS2000 photoelectric measuring system (EVERFINE, China).

2.3. Computation. The crystal structures of Ga_2O_3 and $(Ga_{1.875-x}In_xCr_{0.125})O_3$ (x = 0, 0.0625, 0.125, 0.25, 0.375, 0.5, and 0.625) were optimized using the Vienna Ab initio Simulation Package,[34] which is a plane-wave pseudopotential total energy package based on density functional theory.[35−38] The atomic positions and lattice parameters were relaxed with electronic convergence criteria of 1×10^{-5} eV and atomic convergence criteria of 0.01 eV/Å. The cutoff energy of 500 eV was used for the basis set of the plane waves, and a $4 \times 8 \times 8$ Γ-centered Monkhorst−Pack k-point grid was used to sample the first Brillouin zone. The PBE exchange-correlation functional was employed for structure optimization, charge density, and formation energy calculations, whereas the subsequent electronic properties were determined using the HSE06 hybrid functional.[39]

3. RESULTS AND DISCUSSION

3.1. Phase, Crystal Structure, and Morphology. The powder X-ray diffractograms of $[(Ga_{1.97-x}Cr_{0.03})In_x]O_3$ (x = 0, 0.1, 0.2, 0.3, 0.4, and 0.5), plotted in Figure 1, reveal that the

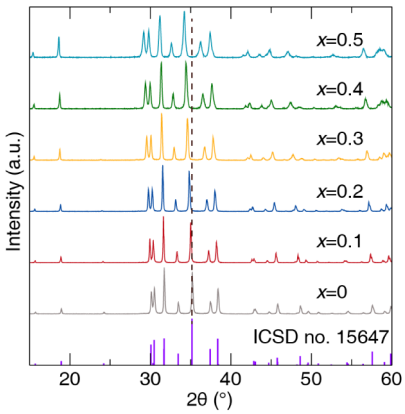

Figure 1. X-ray powder diffractograms of $[(Ga_{1.97-x}Cr_{0.03})In_x]O_3$ (x = 0, 0.1, 0.2, 0.3, 0.4, and 0.5). The standard pattern form of β-Ga_2O_3 (ICSD no. 15 647) is provided.

samples are all phase pure and can be indexed to the β-Ga_2O_3 phase (ICSD no. 15647). A gradual shift of diffraction peaks toward a lower angle follows the increasing concentration of In^{3+} in the product because of the lattice expansion caused by larger In^{3+} ions substituting for the smaller Ga^{3+} ions. The linear change in the refined lattice parameters (Figure S1) follows Vegard's law, indicating the successful incorporation of In^{3+} in the range of x studied without changing the crystal structure. Further increasing In^{3+} beyond x = 0.5 was reported to result in the presence of an In_2O_3 impurity.[33] However, additional procedures in synthesis, including pressing the raw starting materials into a pellet before sintering, resulted in a phase-pure product when x = 0.6 (Figure S2). Unfortunately, the luminescence of the sample when x = 0.6 was very weak. Given the interest in NIR photoluminescence, further values of x were not attempted and additional optical properties from the x = 0.6 sample were not pursued. Rietveld refinements of the X-ray powder diffraction data for $[(Ga_{1.57}Cr_{0.03})In_{0.4}]O_3$ were performed to confirm the crystal structure, with the refinement results shown in Figure 2. The refined crystal structure data are provided in Table 1. The refined atomic positions are provided in Table S1. The β-Ga_2O_3 crystal structure belongs to the monoclinic crystal system with the $C2/m$ (no. 12) space group. The structure is composed of corner-connected distorted octahedral $[(GaO_6]$ and tetrahedral $[GaO_4]$ units that make a three-dimensional polyhedral network, as shown in Figure 3. The Cr^{3+} ion is expected to occupy the octahedral Ga^{3+} site because ionic radii of Ga^{3+} ($r_{6\text{-coord.}}$ = 0.62 Å) is similar to Cr^{3+} ($r_{6\text{-coord.}}$ = 0.615 Å),[40] while In^{3+} appears to enter the octahedral Ga^{3+} site based on the refinement results.

https://doi.org/10.1021/acsami.1c05949
ACS Appl. Mater. Interfaces 2021, 13, 31835−31842

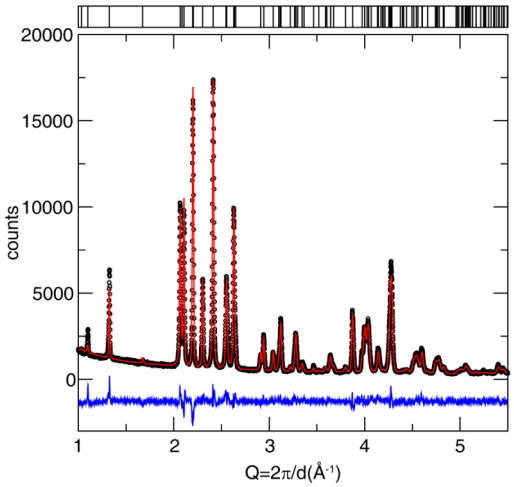

Figure 2. Rietveld refinement of the $[(Ga_{1.57}Cr_{0.03})In_{0.4}]O_3$ X-ray powder diffractogram. The measured data are represented by black circles; the refinement fit is in red, and the difference curve is in blue.

Table 1. Refined Crystal Structure Data

formula	$[(Ga_{1.57}Cr_{0.03})In_{0.4}]O_3$
radiation type; λ (Å)	X-ray; 1.5406
Q range (Å^{-1})	1.000−5.5
temperature (°C)	25
space group; Z	$C2/m$; 2
a (Å)	12.4922(1)
b (Å)	3.1091(1)
c (Å)	5.8740(1)
β (deg)	103.26(3)
unit cell volume (Å^3)	222.05(3)
profile R-factor, R_p	0.0590
weighted profile R-factor, R_{wp}	0.0773
χ^2	7.274

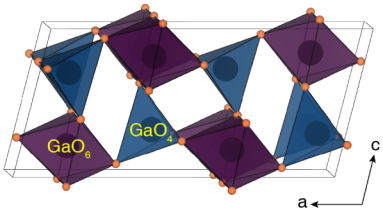

Figure 3. Crystal structure of β-Ga_2O_3 is illustrated with the $[GaO_6]$ and $[GaO_4]$ polyhedral units highlighted.

The morphology of the selected $[(Ga_{1.57}Cr_{0.03})In_{0.4}]O_3$ crystallites as a representative product was then examined using SEM, with a resulting micrograph shown in Figure 4a. The particles form agglomerated columns as their crystal habit, and the average particle size of the materials falls in the 1−6 μm range. EDS mapping (shown in Figure 4b−f) on a randomly selected particle indicates that only the loaded elements (Ga, In, O, and Cr) are present in the sample, with no unexpected elements detected. The elements are also homogeneously distributed throughout the particle. The EDS spectra (Figure S3) reveal that the ratio of atoms In/Ga is 5.91/26.68, which is close to 0.4/1.57, indicating that the nominal composition and EDS-determined chemical composition are consistent.

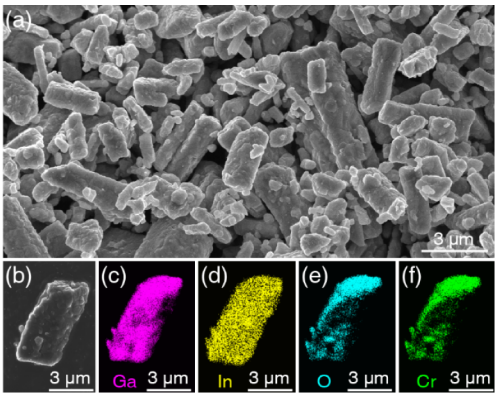

Figure 4. (a) SEM and (b−f) EDS mapping on a single particle of $[(Ga_{1.57}Cr_{0.03})In_{0.4}]O_3$.

3.2. Site Occupation and Electronic Properties. There are two crystallographically independent Ga^{3+} positions in β-Ga_2O_3. One site is tetrahedrally coordinated by oxygen, whereas the second site is octahedrally coordinated by oxygen. Therefore, it is necessary first to identify the site preference of Cr^{3+} and In^{3+} when introduced in the solid solution. The relative formation energies were calculated for each ion type occupying the two different crystallographic positions. The energy difference between these different models was then calculated and is plotted in Figure 5. The calculations show

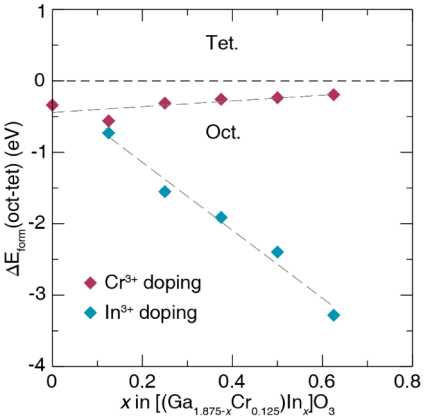

Figure 5. Formation energy differences between octahedral and tetrahedral sites upon the substitution of In^{3+} and Cr^{3+} in $[(Ga_{1.875-x}Cr_{0.125})In_x]O_3$.

that In^{3+} and Cr^{3+} both prefer to enter the octahedral sites rather than tetrahedral sites. This was expected, as noted above, because of the ionic size mismatch effect.[41] Increasing the concentration of In^{3+} in the sample shows that Cr^{3+} always energetically favors the octahedral site. However, adding more In^{3+} decreases the energy difference between the Cr^{3+} occupying the tetrahedral and octahedral sites, while In^{3+} gains an even stronger energy preference to substitute on the octahedral site. Furthermore, the formation energy calculation (Figure S4 and Table S2) of the Cr^{3+}−Cr^{3+} ion pair indicates that Cr^{3+} should be randomly distributed in $(Ga_{1.875}Cr_{0.125})O_3$, whereas In^{3+} incorporation modeled by $[(Ga_{1.8125}Cr_{0.125})$-$In_{0.0625}]O_3$ causes Cr^{3+} to have a strong (≈1 eV/atom) preference to agglomerate instead of separating. Moreover, the deformation charge density calculation (Figure S5) demonstrates that In^{3+} with weaker electronegativity than Ga^{3+} doped

https://doi.org/10.1021/acsami.1c05949
ACS Appl. Mater. Interfaces 2021, 13, 31835−31842

in the Ga_2O_3:Cr^{3+} system partially transfers electrons to the O^{2-} anions surrounding Cr^{3+} and thus changes the local charge distribution of Cr^{3+}, thereby stabilizing the trivalent oxidation state.

To further investigate the influence of dopants on the electronic structure, the density of states (DOSs) of $(Ga_{1.875}Cr_{0.125})O_3$ and $[(Ga_{1.625}Cr_{0.125})In_{0.25}]O_3$ were calculated using the HSE06 hybrid functional. The resulting electronic structures are plotted in Figure 6. The Ga 3d

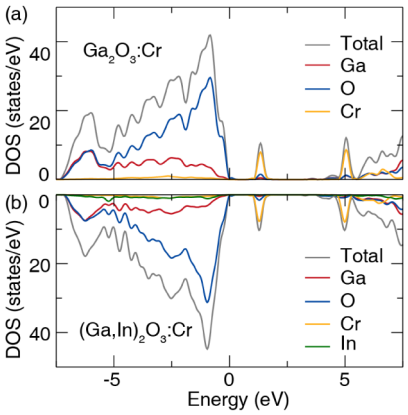

Figure 6. DOSs of (a) $Ga_{1.875}Cr_{0.125}O_3$ and (b) $Ga_{1.625}In_{0.25}Cr_{0.125}O_3$ calculated using the HSE06 hybrid functional.

orbitals set the bottom of the conduction band in $(Ga_{1.875}Cr_{0.125})O_3$, and the O 2p states dominate the top of the valence band. The Cr 3d states are located in the middle of the band gap and are split into occupied t_{2g} states and unoccupied e_g states. The addition of In^{3+} causes the bottom of the conduction band to significantly shift toward lower energy, whereas the t_{2g} and e_g states of Cr^{3+} only shift slightly toward lower energy. This results in the narrowing of the energy gap between the top of valence states and ground states of Cr^{3+}.

3.3. Reflectivity and Band Gap. The DR spectra of $[(Ga_{1.97-x}Cr_{0.03})In_x]O_3$ (x = 0, 0.1, 0.3, and 0.5) were collected and are plotted in Figure 7a. The samples present intense absorption in the blue and red regions of the visible spectrum ascribed to their respective $^4A_2 \rightarrow {}^4T_1$ and $^4A_2 \rightarrow {}^4T_2$ Cr^{3+} electronic transitions. A red shift is observed with increasing In^{3+} content because of the weakening of the crystal field. The

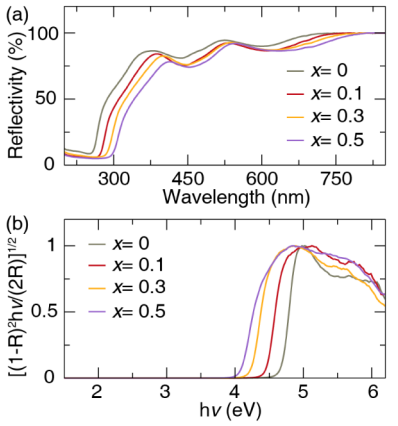

Figure 7. (a) DR spectra of $[(Ga_{1.97-x}Cr_{0.03})In_x]O_3$ (x = 0, 0.1, 0.3, and 0.5) solid solutions and the (b) corresponding optical band gap.

optical band gap (E_g) of these samples can then be estimated for each sample according to the following equation:[42,43]

$$[h\nu\alpha]^{1/n} = A(h\nu - E_g) \quad (1)$$

where $h\nu$, α, E_g, and A refer to the photon energy, absorption coefficient, band gap, and proportionality constant, respectively. The value of the exponent n is determined by the nature of the electronic band and transition type. For the direct allowed transition, direct forbidden transition, indirect allowed transition, and indirect forbidden transition, n values are 1/2, 3/2, 2, and 3, respectively. β-Ga_2O_3 has a direct band gap with an allowed transition (n = 1/2), which results in the optical E_g = 4.75 eV. This is consistent with the reported E_g = 4.78 eV.[44] The band gap was determined to be 4.50, 4.24, and 4.10 eV for x = 0.1, 0.3, and 0.5, respectively, revealing a gradual narrowing band gap with an increase in the In^{3+} concentration (Figure 7b). These experimental results are also in agreement with the computational band gap trends.

3.4. Photoluminescence. The room-temperature photoluminescence excitation and emission spectra of $(Ga_{1.97}Cr_{0.03})$-O_3 are depicted in Figure 8a (gray line). The excitation

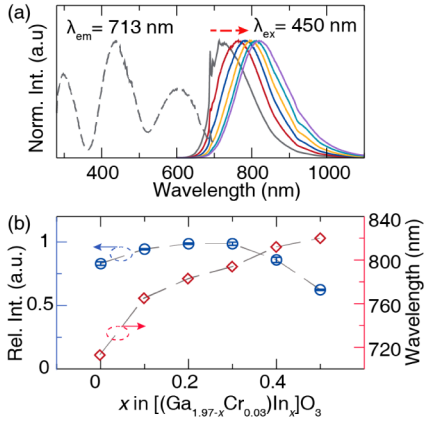

Figure 8. (a) Photoluminescence excitation spectrum of $(Ga_{1.97}Cr_{0.03})O_3$ (dashed line) and photoluminescence emission spectra of $[(Ga_{1.97-x}Cr_{0.03})In_x]O_3$ (x = 0, 0.1, 0.2, 0.3, 0.4, and 0.5). (b) Emission peak wavelength and intensity as a function of In^{3+} concentration, x.

spectrum consists of three broad bands peaking at 297, 437, and 605 nm, corresponding to the $^4A_2 \rightarrow {}^4T_1$ (^4P), $^4A_2 \rightarrow {}^4T_1$ (^4F), and $^4A_2 \rightarrow {}^4T_2$ (^4F) transitions of Cr^{3+}, respectively.[45,46] The excitation spectrum in the visible region is described by two Gaussian peaks, while increasing the In^{3+} concentration produces a significant red-shift in the three bands (Figure S6). This follows the reduction of crystal field splitting, causing a lowering of the energy difference between the $^4A_2$ ground state and the $^4T_1$ (^4P), $^4T_1$ (^4F), and $^4T_2$ (^4F) excited states.[45,47] The crystal field variations can be characterized by crystal field Dq and the Racah parameter, B, calculated using eqs 2−4:[48]

$$10Dq = E(^4T_2) = E(^4A_2 \rightarrow {}^4T_2) \quad (2)$$

$$\frac{Dq}{B} = \frac{15(x-8)}{x^2 - 10x} \quad (3)$$

$$x = \frac{E(^4A_2 \rightarrow {}^4T_1) - E(^4A_2 \rightarrow {}^4T_2)}{Dq} \quad (4)$$

https://doi.org/10.1021/acsami.1c05949
ACS Appl. Mater. Interfaces 2021, 13, 31835−31842

The calculated Dq, B, and Dq/B parameters, presented in Table 2, verify the gradual weakening crystal field strength with increasing In^{3+} concentration.

Table 2. Transition Energy, Crystal Field Parameter, and Racah Parameter for Cr^{3+} in the $[(Ga_{1.97-x}Cr_{0.03})In_x]O_3$ (x = 0, 0.1, 0.2, 0.3, 0.4, and 0.5) Solid Solution

x	$^4A_2-^4T_1$ (cm^{-1})	$^4A_2-^4T_2$ (cm^{-1})	Dq (cm^{-1})	B (cm^{-1})	Dq/B
0	22 883	16 556	1656	624	2.65
0.1	22 675	16 340	1634	627	2.61
0.2	22 573	16 207	1621	633	2.56
0.3	22 321	15 974	1597	633	2.52
0.4	22 222	15 798	1580	646	2.45
0.5	22 124	15 625	1563	659	2.37

The emission spectrum covers a broad region from 650 to 1000 nm, as shown in Figure 8a, extending the emission to a longer wavelength than $(Ga,Sc)_2O_3:Cr^{3+}$ (650–950 nm) as In^{3+} induces weaker crystal field splitting. The weaker crystal field also results in a continuous red-shift of the emission spectra, with the maximum wavelength shifting from 713 to 820 nm as the In^{3+} concentration increases from x = 0 to 0.5. Furthermore, the full width at half-maximum (FWHM) gradually expands from 122 to 157 nm across this same range because of the enhanced electron–phonon coupling.[32] The emission intensity also gradually increases and then decreases, achieving a maximum when x = 0.3 (as shown in Figure 8b). This supports that the initial high efficiency is maintained (or even improved to a point) while making the emission spectrum tunable. This is not often the case for NIR phosphors. The emission intensity enhancement likely stems from the gradual red shift (437–452 nm) of the excitation peak in the blue region, gradually matching better with the 450 nm excitation. Furthermore, the incorporation of In^{3+} may help stabilize Cr^{3+} through charge redistribution and prevent the formation of Cr^{4+}, which is known to act as a luminescence quenching center.[23] However, at a certain point, the high In^{3+} concentration enhances the possibility of nonradiative relaxation by reducing the band gap (Figure 7b). This increases the chance of photoionization by reducing the energy barrier between excited states and the bottom of the conduction band (Figure S7) and increasing electron–phonon coupling, as indicated by the broader emission peak.

The QY of the samples was measured and is listed in Table S3. As shown, when x = 0.4, which has an emission peak wavelength over 800 nm, QY was determined to be 87.9%, with an absorption efficiency of 50.2% (Figure 9). This QY value is close to the highest broadband NIR luminescent material $(Ga,Sc)_2O_3:Cr^{3+}$ (QY ≈ 90%) with an emission peak over 800 nm. The absorption efficiency of this sample is also much higher than previously reported phosphors such as $La_2MgZrO_6:Cr^{3+}$ (32%) and $Gd_3Sc_2Ga_3O_{12}:Cr^{3+}$ (20%).[24,49] For reference, the QY and absorption of $(Ga_{1.97}Cr_{0.3})O_3$ in this work were measured to be 92.5% and 30.7% (Figure S8), respectively, in agreement with the previous report.[31] Obviously, there is a significant absorption increase in this material system with In^{3+} incorporation. Generally, two possible mechanisms can explain the increase in the absorption efficiency of Cr^{3+}-doped phosphor. One approach is to increase the Cr^{3+} concentration to a high level, which occurs in phosphors such as $LaMgGa_{11}O_{19}:Cr^{3+}$.[25] The other mechanism is by introducing odd-parity to break the forbidden

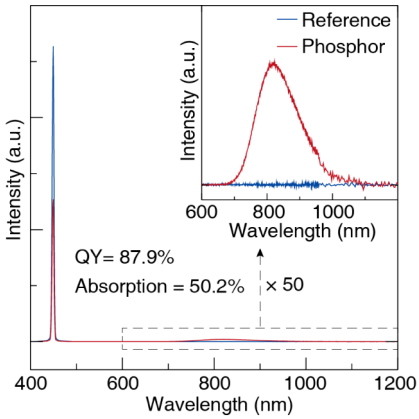

Figure 9. QY measurement of the $[(Ga_{1.57-x}Cr_{0.03})In_{0.4}]O_3$ phosphor under 450 nm excitation. The inset shows the amplified emission spectra and the reference in the 600–1200 nm region.

transitions through lattice distortion.[50] In the reported phosphor here, the Cr^{3+}-doping concentration is low (1.5%) and nearly the same in all samples; hence, the primary mechanism for absorption increase is likely due to the introduction of odd-parity, resulting from a lattice distortion caused by replacing Ga^{3+} ($r_{6\text{-coord.}}$ = 0.62 Å) with larger In^{3+} ($r_{6\text{-coord.}}$ = 0.8 Å).[40]

The room-temperature photoluminescence decay curves of $Ga_{2-x}In_xO_3:Cr^{3+}$ (x = 0–0.5) collected using 450 nm excitation are plotted in Figure 10a. A single exponential

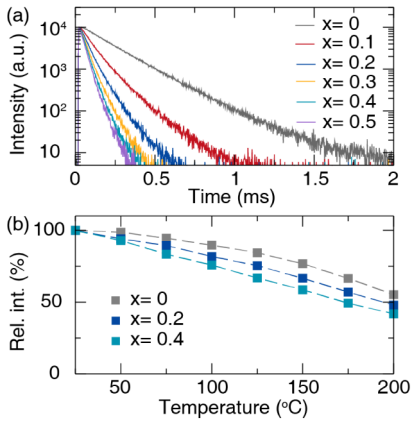

Figure 10. (a) Time-gated photoluminescence decay curves of Cr^{3+} (λ_{ex} = 450 nm) in $[(Ga_{1.97-x}Cr_{0.03})In_x]O_3$ (x = 0, 0.1, 0.2, 0.3, 0.4, and 0.5). (b) Temperature-dependent emission peak intensity of the $[(Ga_{1.97-x}Cr_{0.03})In_x]O_3$ (x = 0, 0.2, and 0.4) samples.

function describes the decay curve of $Ga_2O_3:Cr^{3+}$, as shown in Figure S9, even though the monitored emission peak at 713 nm is composed of spin-forbidden $^2E \rightarrow {}^4A_2$ transitions and spin-allowed $^4T_2 \rightarrow {}^4A_2$ transitions. Because the decay time of spin-allowed $^4T_2 \rightarrow {}^4A_2$ transitions is much shorter than that of spin-forbidden $^2E \rightarrow {}^4A_2$ transitions, the photoluminescence decay time is almost entirely determined by spin-forbidden $^2E \rightarrow {}^4A_2$ transitions in these measurements.[32] Increasing the In^{3+} concentration indicates that the decay curves progressively deviate from the single exponential function, and the lifetimes decrease dramatically. The average lifetimes can be calculated using eq 5:[51,52]

https://doi.org/10.1021/acsami.1c05949
ACS Appl. Mater. Interfaces 2021, 13, 31835–31842

$$\bar{\tau} = \frac{\int_0^{t_{max}} tI(t)\,dt}{\int_0^{t_{max}} I(t)\,dt} \quad (5)$$

where 0 and t_{max} are the time of beginning and end of the measurement range, respectively, and $I(t)$ is the intensity of luminescence at time t. The calculated average lifetimes are 230.1 μs (x = 0), 122.0 μs (x = 0.1), 85.0 μs (x = 0.2), 67.0 μs (x = 0.3), 64.2 μs (x = 0.4), and 57.8 μs (x = 0.5). The decrease in the luminescence lifetimes with an increase in In^{3+} concentration likely stems from the disappearance of the spin-forbidden $^2E \rightarrow {}^4A_2$ transitions, while the decay curves gradually deviating from a single exponential function is mainly ascribed to the site distortion with increasing In^{3+} concentration.

The temperature-dependent photoluminescence of $[(Ga_{1.97-x}Cr_{0.03})In_x]O_3$ (x = 0, 0.2, and 0.4) was also evaluated. The emission peak intensity as a function of temperature is shown in Figure 10b and indicates that the emission intensity decreases with increasing temperature in all samples. The emission intensity at 150 °C remains high (77%) for the unsubstituted sample and then decreases to 66% when x = 0.2 and to 60% when x = 0.4. The value for sample x = 0.4 is lower than that for $LiInSi_2O_6:Cr^{3+}$ (77%)[7] but higher than those for $Ca_2LuScGa_2Ge_2O_{12}:Cr^{3+}$ (59%),[45] $ScBO_3:Cr^{3+}$ (51%),[8] and $LiIn_2SbO_6:Cr^{3+}$ (<10%) phosphors,[30] which have an emission peak over 800 nm. The change in the thermal stability with more In^{3+} is due to the gradually enhanced electron−phonon coupling effect, making the phonon-assisted cross-relaxation between the excited and ground states easier, which is supported by the significant increasing of the Huang−Rhys factor (S) as In^{3+} concentration increases (Figure S10),[20] while the reduced host band gap promotes the possibility of photoionization thermal quenching.[53,54] Besides, the narrowing of the band gap between the top of valence states and ground states of Cr^{3+} may also promote the possibility of valence electrons entering into ground states and preventing radiative transitions of excited electrons back to ground states, which also occurs in Mn^{4+}-activated phosphors.[55]

3.5. Application to pc-NIR LEDs. Given the excellent optical properties of $[(Ga_{1.97-x}Cr_{0.03})In_x]O_3$, especially compared to overall Cr^{3+} phosphors reported thus far, a prototype of a pc-NIR LED device (shown in the inset of Figure 11a) was fabricated by combining the optimal phosphor, $[(Ga_{1.57}Cr_{0.03})In_{0.4}]O_3$, with a 450 nm blue InGaN chip. The fabricated LED device was driven by 30−300 mA, which produced an emission peak centered at 820 nm with an FWHM of 150 nm (Figure 11a). Increasing the current from 30 to 300 mA, as plotted in Figure 11b, shows that the output power gradually increases from 21 to 154.8 mW without saturating, indicating that higher output power could be achieved using an even high power excitation light source. The photoelectric conversion efficiency gradually decreases from 26.6% to 17.2% and would also likely be even better if the data above 1000 nm were included in the calculation.

The NIR light constructed was then used in addition to a standard LED light bulb to illuminate various produce. Figure 11c shows the photographs obtained by different cameras under natural light and pc-NIR LED light. The visible-light camera shows a conventional color photo illuminated by a standard light (Figure 11c, left). Turning on the pc-NIR LED and using the same visible-light camera (Figure 11c, center) do not show any image. In contrast, the NIR camera can capture

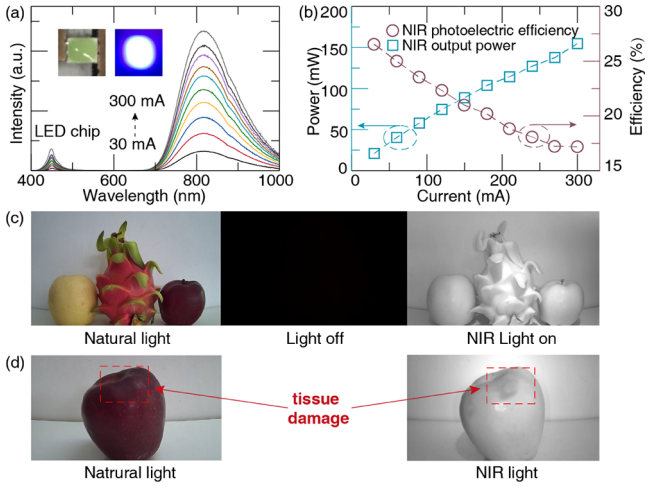

Figure 11. (a) Photoluminescence spectrum of the fabricated pc-NIR LED device that combines a 450 nm InGaN blue LED chip (λ_{em} = 450 nm) with $[(Ga_{1.57}Cr_{0.03})In_{0.4}]O_3$ NIR phosphor under a forward bias of 30−300 mA, and the insets show the photographs of the LED device. (b) Output power and photoelectric conversion efficiency of NIR device as a function of driven current in the range of 30−300 mA. (c) Photographs under natural light and pc-NIR LED light captured by the corresponding visible camera and an NIR camera. (d) Photographs of tissue damage under natural light and pc-NIR LED light captured by the corresponding visible camera and an NIR camera.

black-and-white images when the pc-NIR LED lamp is illuminated. Most importantly, the NIR camera can also detect the tissue damage of fruit, which is not easily detected by the naked eye or a standard visible-light camera (Figure 11d). These results substantiate the phosphor system's outstanding photoelectric conversion efficiency and its great potential in NIR LED applications.

4. CONCLUSIONS

In summary, a series of broadband NIR Cr^{3+}-substituted $[(Ga_{1.97-x}Cr_{0.03})In_x]O_3$ solid solution phosphors with a high efficiency and tunable emission were successfully synthesized via a high-temperature solid-state reaction. The phase purity was confirmed by powder X-ray diffraction and supported by electron microscopy. Formation energy calculations revealed that the In^{3+} and Cr^{3+} ions prefer to occupy the octahedral crystallographic site rather than the tetrahedrally coordinated Ga^{3+} position. The reflectivity measurement indicates that upon In^{3+} substitution, the absorption of Cr^{3+} red-shifts and a steady reduction of the band gap from 4.75 to 4.10 eV occurs. The photoluminescence results confirm the photoluminescence excitation, emission spectra also red-shift with a high In^{3+} content because of the weakening crystal field strength, and ultrahigh QY (87.9% for x = 0.4) and absorption efficiency (50.2% for x = 0.4) of this material system can be achieved in a broad emission region (713−820 nm). Finally, under a driving current of 60 mA, the output power and photoelectric conversion efficiency of a prototype of a pc-NIR LED device fabricated using a 450 nm LED combined with the as-prepared $[(Ga_{1.57}Cr_{0.03})In_{0.4}]O_3$ phosphor reached 40.4 mW and 25.0%, respectively, making the device fabrication using this phosphor competitive with the best materials currently available for NIR LED applications.

https://doi.org/10.1021/acsami.1c05949
ACS Appl. Mater. Interfaces 2021, 13, 31835−31842

■ ASSOCIATED CONTENT

Supporting Information

The Supporting Information is available free of charge at https://pubs.acs.org/doi/10.1021/acsami.1c05949.

Lattice parameters, X-ray powder diffractograms, EDS spectra, computational models, deformation charge density, excitation spectra, energy levels diagram, QY, decay curve, Huang−Rhys factor, atomic positions, and formation energy (PDF)

■ AUTHOR INFORMATION

Corresponding Authors

Weiren Zhao − *School of Physics and Optoelectronic Engineering, Guangdong University of Technology, Guangzhou 510006, China*; Email: zwren123@126.com

Jakoah Brgoch − *Department of Chemistry, University of Houston, Houston, Texas 77204, United States*; orcid.org/0000-0002-1406-1352; Email: jbrgoch@uh.edu

Fu Du − *School of Metallurgy and Chemistry Engineering, Jiangxi University of Science and Technology, Ganzhou 341000, China*; Email: dufu0403@sina.com

Authors

Jiyou Zhong − *School of Physics and Optoelectronic Engineering, Guangdong University of Technology, Guangzhou 510006, China*; orcid.org/0000-0003-2817-6617

Ya Zhuo − *Department of Chemistry, University of Houston, Houston, Texas 77204, United States*; orcid.org/0000-0003-2554-498X

Hongshi Zhang − *School of Physics and Optoelectronic Engineering, Guangdong University of Technology, Guangzhou 510006, China*

Complete contact information is available at: https://pubs.acs.org/10.1021/acsami.1c05949

Notes

The authors declare no competing financial interest.

■ ACKNOWLEDGMENTS

The authors thank the National Natural Science Foundation of China (no. 51702057) and the National Science Foundation (DMR-1847701). This research used the Maxwell/Opuntia/Sabine cluster(s) operated by the University of Houston and the Research Computing Data Core (RCDC).

■ REFERENCES

(1) Grassi, B.; Quaresima, V. Near-Infrared Spectroscopy and Skeletal Muscle Oxidative Function in Vivo in Health and Disease: A Review from an Exercise Physiology Perspective. *J. Biomed. Opt.* **2016**, *21*, No. 091313.

(2) Scholkmann, F.; Kleiser, S.; Metz, A. J.; Zimmermann, R.; Mata Pavia, J.; Wolf, U.; Wolf, M. A Review on Continuous Wave Functional Near-Infrared Spectroscopy and Imaging Instrumentation and Methodology. *NeuroImage* **2014**, *85*, 6−27.

(3) Manley, M. Near-Infrared Spectroscopy and Hyperspectral Imaging: Non-Destructive Analysis of Biological Materials. *Chem. Soc. Rev.* **2014**, *43*, 8200−8214.

(4) Magwaza, L. S.; Opara, U. L.; Nieuwoudt, H.; Cronje, P. J. R.; Saeys, W.; Nicolaï, B. NIR Spectroscopy Applications for Internal and External Quality Analysis of Citrus Fruit-A Review. *Food Bioprocess Technol.* **2012**, *5*, 425−444.

(5) Huang, L.; Lin, L.; Xie, W.; Qiu, Z.; Ni, H.; Liang, H.; Tang, Q.; Cao, L.; Meng, J. X.; Li, F. Near-Infrared Persistent Luminescence in a Cr3+-Doped Perovskite for Low-Irradiance Imaging. *Chem. Mater.* **2020**, *32*, 5579−5588.

(6) Lucero, A. A.; Addae, G.; Lawrence, W.; Neway, B.; Credeur, D. P.; Faulkner, J.; Rowlands, D.; Stoner, L. Reliability of Muscle Blood Flow and Oxygen Consumption Response from Exercise Using Near-Infrared Spectroscopy. *Exp. Physiol.* **2018**, *103*, 90−100.

(7) Xu, X.; Shao, Q.; Yao, L.; Dong, Y.; Jiang, J. Highly Efficient and Thermally Stable Cr3+-Activated Silicate Phosphors for Broadband near-Infrared LED Applications. *Chem. Eng. J.* **2020**, *383*, No. 123108.

(8) Shao, Q.; Ding, H.; Yao, L.; Xu, J.; Liang, C.; Jiang, J. Photoluminescence Properties of a ScBO3: Cr3+Phosphor and Its Applications for Broadband near-Infrared LEDs. *RSC Adv.* **2018**, *8*, 12035−12042.

(9) Huang, W.-T.; Cheng, C.-L.; Bao, Z.; Yang, C.-W.; Lu, K.-M.; Kang, C.-Y.; Lin, C.-M.; Liu, R.-S. Broadband Cr^{3+},Sn^{4+}-Doped Oxide Nanophosphors for Infrared Mini Light-Emitting Diodes. *Angew. Chem.* **2018**, *131*, No. 201813340.

(10) Gao, T.; Zhuang, W.; Liu, R.; Liu, Y.; Yan, C.; Chen, X. Design of a Broadband NIR Phosphor for Security-Monitoring LEDs: Tunable Photoluminescence Properties and Enhanced Thermal Stability. *Cryst. Growth Des.* **2020**, *20*, 3851−3860.

(11) Guzman, G. N. A. D.; Rajendran, V.; Bao, Z.; Fang, M. H.; Pang, W. K.; Mahlik, S.; Lesniewski, T.; Grinberg, M.; Molokeev, M. S.; Leniec, G.; Kaczmarek, S. M.; Ueda, J.; Lu, K. M.; Hu, S. F.; Chang, H.; Liu, R. S. Multi-Site Cation Control of Ultra-Broadband Near-Infrared Phosphors for Application in Light-Emitting Diodes. *Inorg. Chem.* **2020**, *59*, 15101−15110.

(12) Zhao, M.; Zhang, Q.; Xia, Z. Structural Engineering of Eu 2+ -Doped Silicates Phosphors for LED Applications. *Acc. Mater. Res.* **2020**, *1*, 137−145.

(13) Xia, Z.; Liu, Q. Progress in Materials Science Progress in Discovery and Structural Design of Color Conversion Phosphors for LEDs. *Prog. Mater. Sci.* **2016**, *84*, 59−117.

(14) Li, G.; Tian, Y.; Zhao, Y.; Lin, J. Recent Progress in Luminescence Tuning of Ce3+ and Eu2+-Activated Phosphors for Pc-WLEDs. *Chem. Soc. Rev.* **2015**, *44*, 8688−8713.

(15) De Guzman, G. N. A.; Fang, M.-H.; Liang, C.-H.; Bao, Z.; Hu, S.-F.; Liu, R.-S. [INVITED] Near-Infrared Phosphors and their Full Potential: A Review on Practical Applications and Future Perspectives. *J. Lumin.* **2020**, *219*, No. 116944.

(16) Yao, L.; Shao, Q.; Han, S.; Liang, C.; He, J.; Jiang, J. Enhancing Near-Infrared Photoluminescence Intensity and Spectral Properties in Yb3+ Codoped LiScP2O7: Cr3+. *Chem. Mater.* **2020**, *32*, 2430−2439.

(17) You, L.; Tian, R.; Zhou, T.; Xie, R. Broadband Near-Infrared Phosphor BaMgAl10O17: Cr3+ Realized by Crystallographic Site Engineering. *Chem. Eng. J.* **2021**, *417*, No. 129224.

(18) Malysa, B.; Meijerink, A.; Jüstel, T. Temperature Dependent Photoluminescence of Cr3+ Doped Sr8MgLa(PO4)7. *Opt. Mater. (Amsterdam, Neth.)* **2018**, *85*, 341−348.

(19) Xie, W.; Jiang, W.; Zhou, R.; Li, J.; Ding, J.; Ni, H.; Zhang, Q.; Tang, Q.; Meng, J.-X.; Lin, L. Disorder-Induced Broadband Near-Infrared Persistent and Photostimulated Luminescence in Mg2SnO4: Cr3+. *Inorg. Chem.* **2021**, *60*, 2219−2227.

(20) Song, E.; Ming, H.; Zhou, Y.; He, F.; Wu, J.; Xia, Z.; Zhang, Q. Cr3+-Doped Sc-Based Fluoride Enabling Highly Efficient Near Infrared Luminescence: A Case Study of K2NaScF6: Cr3+. *Laser Photonics Rev.* **2021**, *15*, No. 2000410.

(21) Zhang, L.; Zhang, S.; Hao, Z.; Zhang, X.; Pan, G. H.; Luo, Y.; Wu, H.; Zhang, J. A High Efficiency Broad-Band near-Infrared Ca2LuZr2Al3O12: Cr3+Garnet Phosphor for Blue LED Chips. *J. Mater. Chem. C* **2018**, *6*, 4967−4976.

(22) Malysa, B.; Meijerink, A.; Jüstel, T. Temperature Dependent Cr3+ Photoluminescence in Garnets of the Type X3Sc2Ga3O12 (X = Lu, Y, Gd, La). *J. Lumin.* **2018**, *202*, 523−531.

(23) Jia, Z.; Yuan, C.; Liu, Y.; Wang, X.-J.; Sun, P.; Wang, L.; Jiang, H.; Jiang, J. Strategies to Approach High Performance in Cr3+-Doped

Phosphors for High-Power NIR-LED Light Sources. *Light: Sci. Appl.* **2020**, *9*, No. 86.
(24) Basore, E. T.; Xiao, W.; Liu, X.; Wu, J.; Qiu, J. Broadband Near-Infrared Garnet Phosphors with Near-Unity Internal Quantum Efficiency. *Adv. Opt. Mater.* **2020**, *8*, 1−5.
(25) Liu, S.; Wang, Z.; Cai, H.; Song, Z.; Liu, Q. Highly Efficient Near-Infrared Phosphor LaMgGa11O19: Cr3+. *Inorg. Chem. Front.* **2020**, *7*, 1467−1473.
(26) Lai, J.; Zhou, J.; Long, Z.; Qiu, J.; Zhou, D.; Yang, Y.; Zhang, K.; Shen, W.; Wang, Q. Broadband Near-Infrared Emitting from Li1.6Zn1.6Sn2.8O8: Cr3+Phosphor by Two-Site Occupation and Al3+ Cationic Regulation. *Mater. Des.* **2020**, *192*, No. 108701.
(27) Zhao, F.; Song, Z.; Zhao, J.; Liu, Q. Double Perovskite Cs2AgInCl6: Cr3+:Broadband and near-Infrared Luminescent Materials. *Inorg. Chem. Front.* **2019**, *6*, 3621−3628.
(28) Wang, C.; Wang, X.; Zhou, Y.; Zhang, S.; Li, C.; Hu, D.; Xu, L.; Jiao, H. An Ultra-Broadband Near-Infrared Cr3+ -Activated Gallogermanate Mg3Ga2GeO8 Phosphor as Light Sources for Food Analysis. *ACS Appl. Electron. Mater.* **2019**, *1*, 1046−1053.
(29) Lai, J.; Shen, W.; Qiu, J.; Zhou, D.; Long, Z.; Yang, Y.; Zhang, K.; Khan, I.; Wang, Q. Broadband Near-Infrared Emission Enhancement in K2Ga2Sn6O16: Cr3+Phosphor by Electron-Lattice Coupling Regulation. *J. Am. Ceram. Soc.* **2020**, *103*, 5067−5075.
(30) Liu, G.; Hu, T.; Molokeev, M. S.; Xia, Z. Li/Na Substitution and Yb3+ Co-Doping Enabling Tunable near-Infrared Emission in LiIn2SbO6: Cr3+Phosphors for Light-Emitting Diodes. *iScience* **2021**, *24*, No. 102250.
(31) Fang, M. H.; De Guzman, G. N. A.; Bao, Z.; Majewska, N.; Mahlik, S.; Grinberg, M.; Leniec, G.; Kaczmarek, S. M.; Yang, C. W.; Lu, K. M.; Sheu, H. S.; Hu, S. F.; Liu, R. S. Ultra-High-Efficiency near-Infrared Ga2O3: Cr3+Phosphor and Controlling of Phytochrome. *J. Mater. Chem. C* **2020**, *8*, 11013−11017.
(32) Fang, M.-H.; Chen, K.-C.; Majewska, N.; Leśniewski, T.; Mahlik, S.; Leniec, G.; Kaczmarek, S. M.; Yang, C.-W.; Lu, K.-M.; Sheu, H.-S.; Liu, R.-S. Hidden Structural Evolution and Bond Valence Control in Near-Infrared Phosphors for Light-Emitting Diodes. *ACS Energy Lett.* **2021**, *6*, 109−114.
(33) Baldini, M.; Gogova, D.; Irmscher, K.; Schmidbauer, M.; Wagner, G.; Fornari, R. Heteroepitaxy of Ga2(1-x)In2xO3 Layers by MOVPE with Two Different Oxygen Sources. *Cryst. Res. Technol.* **2014**, *49*, 552−557.
(34) Hafner, J. Ab-Initio Simulations of Materials Using VASP: Density-Functional Theory and Beyond. *J. Comput. Chem.* **2008**, *29*, 2044−2078.
(35) Hohenberg, P.; Kohn, W. Inhomogeneous Electron Gas. *Phys. Rev.* **1964**, *136*, B864−B871.
(36) Kohn, W.; Sham, L. J. Self-Consistent Equations Including Exchange and Correlation Effects. *Phys. Rev.* **1965**, *140*, A1133−A1138.
(37) Kresse, G.; Hafner, J. Ab Initio Molecular Dynamics for Liquid Metals. *Phys. Rev. B: Condens. Matter Mater. Phys.* **1993**, *47*, 558−561.
(38) Kresse, G.; Furthmüller, J. Efficient Iterative Schemes for Ab Initio Total-Energy Calculations Using a Plane-Wave Basis Set. *Phys. Rev. B: Condens. Matter Mater. Phys.* **1996**, *54*, 11169−11186.
(39) Heyd, J.; Scuseria, G. E.; Ernzerhof, M. Hybrid Functionals Based on a Screened Coulomb Potential. *J. Chem. Phys.* **2003**, *118*, 8207−8215.
(40) Shannon, R. D. Revised Effective Ionic Radii and Systematic Studies of Interatomic Distances in Halides and Chalcogenides. *Acta Crystallogr., Sect. A: Found. Crystallogr.* **1976**, *32*, 751−767.
(41) Chen, W. T.; Sheu, H. S.; Liu, R. S.; Attfield, J. P. Cation-Size-Mismatch Tuning of Photoluminescence in Oxynitride Phosphors. *J. Am. Chem. Soc.* **2012**, *134*, 8022−8025.
(42) Tauc, J.; Grigorovici, R.; Vancu, A. Optical Properties and Electronic Structure of Amorphous Germanium. *Phys. Status Solidi* **1966**, *15*, 627−637.
(43) Makuła, P.; Pacia, M.; Macyk, W. How To Correctly Determine the Band Gap Energy of Modified Semiconductor Photocatalysts Based on UV-Vis Spectra. *J. Phys. Chem. Lett.* **2018**, *9*, 6814−6817.
(44) Makeswaran, N.; Battu, A. K.; Swadipta, R.; Manciu, F. S.; Ramana, C. V. Spectroscopic Characterization of the Electronic Structure, Chemical Bonding, and Band Gap in Thermally Annealed Polycrystalline Ga 2 O 3 Thin Films. *ECS J. Solid State Sci. Technol.* **2019**, *8*, Q3249−Q3253.
(45) Bai, B.; Dang, P.; Huang, D.; Lian, H.; Lin, J. Broadband Near-Infrared Emitting Ca2LuScGa2Ge2O12: Cr3+Phosphors: Luminescence Properties and Application in Light-Emitting Diodes. *Inorg. Chem.* **2020**, *59*, 13481−13488.
(46) Liu, G.; Molokeev, M. S.; Lei, B.; Xia, Z. Two-Site Cr3+ Occupation in the MgTa2O6: Cr3+Phosphor toward Broad-Band near-Infrared Emission for Vessel Visualization. *J. Mater. Chem. C* **2020**, *8*, 9322−9328.
(47) Finley, E.; Brgoch, J. Deciphering the Loss of Persistent Red Luminescence in ZnGa2O4: Cr3+upon Al3+ Substitution. *J. Mater. Chem. C* **2019**, *7*, 2005−2013.
(48) Struve, B.; Huber, G. The Effect of the Crystal Field Strength on the Optical Spectra of Cr3+ in Gallium Garnet Laser Crystals. *Appl. Phys. B: Photophys. Laser Chem.* **1985**, *36*, 195−201.
(49) Zeng, H.; Zhou, T.; Wang, L.; Xie, R. J. Two-Site Occupation for Exploring Ultra-Broadband Near-Infrared Phosphor - Double-Perovskite La2MgZrO6: Cr3+. *Chem. Mater.* **2019**, *31*, 5245−5253.
(50) Payne, S. A.; Chase, L. L.; Wilke, G. D. Optical Spectroscopy of the New Laser Materials, LiSrAlF6: Cr3+and LiCaAlF6: Cr3+. *J. Lumin.* **1989**, *44*, 167−176.
(51) Lee, C.; Bao, Z.; Fang, M. H.; Lesniewski, T.; Mahlik, S.; Grinberg, M.; Leniec, G.; Kaczmarek, S. M.; Brik, M. G.; Tsai, Y. T.; Tsai, T. L.; Liu, R.-S. Chromium(III)-Doped Fluoride Phosphors with Broadband Infrared Emission for Light-Emitting Diodes. *Inorg. Chem.* **2020**, *59*, 376−385.
(52) Xia, Z.; Liu, R. Tunable Blue-Green Color Emission and Energy Transfer of Ca2Al3O6F:Ce3+,Tb3+ Phosphors for Near-UV White LEDs. *J. Phys. Chem. C* **2012**, *116*, 15604−15609.
(53) Zhong, J.; Zhuang, W.; Xing, X.; Liu, R.; Li, Y.; Liu, Y.; Hu, Y. Synthesis, Crystal Structures, and Photoluminescence Properties of Ce3+-Doped Ca2LaZr2Ga3O12: New Garnet Green-Emitting Phosphors for White Leds. *J. Phys. Chem. C* **2015**, *119*, 5562−5569.
(54) Zhong, J.; Zhao, W.; Du, F.; Wen, J.; Zhuang, W.; Liu, R.; Duan, C. K.; Wang, L.; Lin, K. Identifying the Emission Centers and Probing the Mechanism for Highly Efficient and Thermally Stable Luminescence in the La3Si6N11: Ce3+Phosphor. *J. Phys. Chem. C* **2018**, *122*, 7849−7858.
(55) Wang, L.; Dai, Z.; Zhou, R.; Qu, B.; Zeng, X. C. Understanding the Quenching Nature of Mn4+ in Wide Band Gap Inorganic Compounds: Design Principles for Mn4+ Phosphors with Higher Efficiency. *Phys. Chem. Chem. Phys.* **2018**, *20*, 16992−16999.

https://doi.org/10.1021/acsami.1c05949
ACS Appl. Mater. Interfaces 2021, 13, 31835−31842